

Document downloaded from:

<http://hdl.handle.net/10251/167326>

This paper must be cited as:

Barrio, J.; Cucarella, N.; González Martínez, AJ.; Freire, M.; Ilisie, V.; Benloch Baviera, JM. (2020). Characterization of a High-Aspect Ratio Detector With Lateral Sides Readout for Compton PET. IEEE Transactions on Radiation and Plasma Medical Sciences. 4(5):546-554. <https://doi.org/10.1109/TRPMS.2020.3006862>



The final publication is available at

<https://doi.org/10.1109/TRPMS.2020.3006862>

Copyright Institute of Electrical and Electronics Engineers

Additional Information

# Characterization of a high aspect ratio detector with lateral sides readout for Compton PET

John Barrio, Neus Cucarella, Antonio J. Gonzalez, *Member, IEEE*, Marta Freire, Victor Ilisie, and Jose M. Benlloch

**Abstract**—Although Positron Emission Tomography is probably the most specific molecular imaging modality, it still lacks of a high detection sensitivity. One way of improving this is by implementing larger axial scanners and, therefore, increasing the solid angle coverage. Alternatively, it is possible to increase the sensitivity gain by improving the timing capabilities of the detectors. However, from the most fundamental nature of particle interactions with matter, the 511 keV gamma-rays suffer, in most of the cases, from scatter collisions either in the patient or within the detector block, before a photoelectric event eventually occurs. Recovering all scattered (Compton) events would improve scanner sensitivity. In this work we show the performance of a detector block geometry suitable for the development of PET scanners based on several detector layers. A geometry using multiple layers favor the process of scattered events, at the time that allows one for their proper identification. The detector block consists of a LYSO crystal with  $51.5 \times 51.5$  mm<sup>2</sup> surface and 3 mm thickness, resulting in a very high aspect ratio above 17. Four custom-made SiPM arrays of  $1 \times 16$  elements with  $3 \times 3$  mm<sup>2</sup> area each are coupled to the lateral sides of the crystal. Four different methods to estimate the gamma-ray interaction position using the information collected by the four SiPM arrays have been implemented and compared in order to assess the most suitable one for this detector configuration and aspect ratio. A novel calibration method based on Voronoi diagrams has been successfully implemented, allowing us to recover data for the entire detector block. We have reached an intrinsic spatial resolution for the whole block of less than 1.6 mm FWHM, combined with an energy resolution of 12.1%. We have also compared the performance results with detector blocks using the same crystal but employing the standard backreading approach. Similar results were obtained but making use of 4 times less SiPM active area in the case of the lateral reading compared to the backreading method, and with the possibility to minimize the undesirable scatter in the photosensor layers.

**Index Terms**— high aspect ratio, lateral readout, PET, scintillation crystal, SiPM.

## I. INTRODUCTION

**S**ENSITIVITY of commercial Positron Emission Tomography (PET) scanners is very low, of the order of 1% [1][2]. This is due to two main factors: axial coverage is limited and Compton events are discarded. Other factors such as the scintillator thickness also play a role, but less significant to the large number of Compton events. Recovering these events and

including them into the image reconstruction would improve the image quality through both the signal-to-noise ratio and the system sensitivity [3]. Current PET technology focuses on detecting photoelectric events due to the fact that the position of the first interaction in Compton events is unknown. Moreover, it is not possible to distinguish Compton events in the detector from Compton events occurring inside the body of the patient. For this reason, events that lie outside the photoelectric peak are rejected as they produce noise and blurring in the image.

Compton events have been used in the past by Silicon or Cadmium-Telluride based Compton cameras [4][5], due to the excellent energy resolution of semiconductor technology. However, their time resolution is, in most of the cases, limited and it does not allow for a sequential analysis of the whole gamma ray interactions. Detector blocks based on fast scintillation crystals can overcome this limitation.

Detectors based on multiple crystal layers allow layer-independent interactions and, thus, separating Compton and photoelectric events. Another advantage of these detectors is that the depth-of-interaction (DOI) information can be directly obtained identifying the layer in which the interaction took place. In these cases, the DOI resolution is determined by the layer thickness. One approach of this detector concept is to stack multiple layers with the minimum separation between layers or even no separation in one detector module. In particular, in [6], the authors developed a prototype detector based on CsI(Tl) with layers of dimensions  $27.4 \times 27.4 \times 3$  mm<sup>3</sup> (aspect ratio of 9.1). A similar concept was carried out based on LYSO crystals [7] but with smaller layer dimensions of  $13.34 \times 13.34 \times 2.75$  mm<sup>3</sup> (aspect ratio 4.8).

In this work we present a detector block design for PET systems intended for multiple separated crystal layers, so each layer can work as a stand-alone PET detector (photoelectric) or as a plane of a Compton camera. We envisaged the use of very high aspect ratio crystal configurations based on LYSO [8]. We have selected a crystal design with entrance and exit faces of the gamma-ray radiation of conventional dimensions of  $51.5 \times 51.5$  mm<sup>2</sup> and a thickness of only 3 mm, resulting in a high aspect ratio of 17.2, which is significantly larger than previous experimental works [6][7]. The dimensions of our

This project has received funding from the European Research Council (ERC) under the European Union's Horizon 2020 research and innovation program (grant agreement No 695536).

J. Barrio, N. Cucarella, A.J. Gonzalez, M. Freire, V. Ilisie and J.M. Benlloch are with Instituto de Instrumentación para Imagen Molecular (I3M), Centro Mixto CSIC — Universitat Politècnica de València, Camino de Vera s/n, 46022 Valencia, Spain (e-mail: jbarrio@i3m.upv.es).

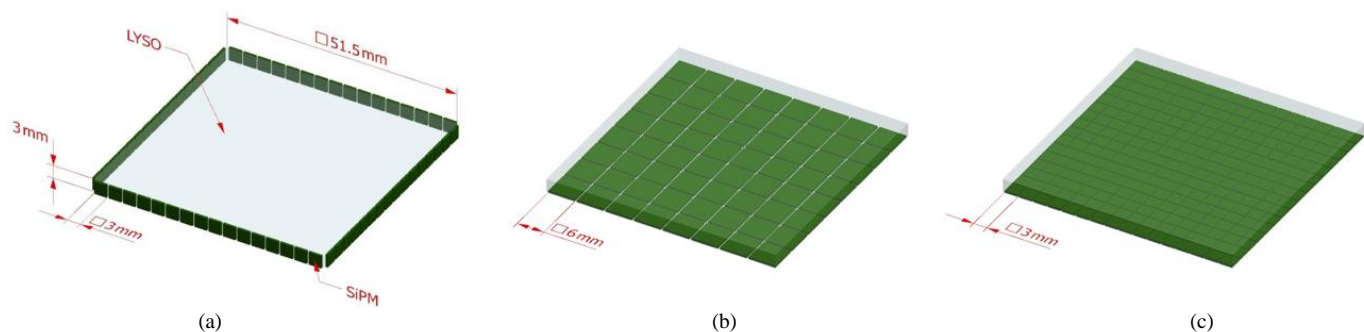


Fig. 1. Sketches of the different detector configurations: (a) lateral sides readout employing 4 arrays of  $1 \times 16$  SiPMs, (b) backreading readout employing a  $8 \times 8$  SiPMs array and (c) backreading readout employing a  $16 \times 16$  SiPMs array.

detector make them suitable for both whole or total-body PET, but also to organ-dedicated PET systems [9]. Notice that wide surface areas increase sensitivity, and thin lateral walls reduce multiple interactions within a single layer. Moreover, the readout and characterization of the gamma rays is done by detecting scintillation photons on the four lateral faces. In this case, this translates into coupling the photosensors to the  $51.5 \times 3$  mm<sup>2</sup> sides. With this approach, the total amount of photosensor material (per layer) can be reduced compared to the traditional coupling to one of the large faces of the crystal.

In this work, four different methods to estimate the interaction position based on the center of gravity algorithm have been implemented and compared in order to assess the most suitable one for this detector configuration and aspect ratio. The center of gravity algorithm is easier to implement compared to other approaches as suggested in [7] for large aspect ratio designs. Also, a novel calibration method for energy and planar coordinates based on Voronoi diagrams has been successfully implemented. The performance of the detector has been evaluated in terms of energy and spatial resolution and furthermore compared to the standard backreading approach.

## II. MATERIALS AND METHODS

### A. Materials

We have used two LYSO slabs (Proteus, Ohio, USA) with  $51.5 \times 51.5 \times 3$  mm<sup>3</sup> dimensions (aspect ratio 17.2), having all faces polished, and ESR (Enhanced Specular Reflector) films added to the two large faces of the crystal. In a second set of experiments and for comparison purposes, the treatment applied to those same two LYSO crystals was modified, in order to read the scintillation light using one of the large  $51.5 \times 51.5$  mm<sup>2</sup> faces. In this case, the lateral faces and the remaining large face were also covered with ESR layers.

During the tests performed with the lateral reading approach, each side face of the crystals was read out using custom-made SiPM arrays of  $1 \times 16$  elements, with  $3 \times 3$  mm<sup>2</sup> active area each. The SiPMs were of the J-Series type (35 microns cell size) from SensL (now On-Semi) with a pitch of 3.21 mm, see Fig. 1 (a). Two more SiPM array configurations have been used when reading the LYSO slabs through the large faces, named as backreading in this work. In particular, we used two standard arrays of  $8 \times 8$  SiPMs from SensL (J-Series type) with  $6 \times 6$  mm<sup>2</sup>

each and a pitch of 6.33 mm (Fig. 1 (b)), and two custom arrays of  $16 \times 16$  SiPMs but with  $3 \times 3$  mm<sup>2</sup> active area each and a pitch of 3.26 mm [10] (Fig. 1 (c)), both covering about  $50 \times 50$  mm<sup>2</sup> active area. The coupling of the SiPMs to the scintillators was performed using optical grease (Bluesil Past 7).

In order to ensure the proper alignment of the different configurations, both crystals and SiPMs were assembled together using 3D printed housings with accurate positioning in the range of 200 microns, see Fig. 2 (a).

The performance study of the crystal and photosensor assemblies was carried out using two different arrays of <sup>22</sup>Na sources. An array of  $11 \times 11$  sources (total activity of 12.5  $\mu$ Ci) with 1 mm in diameter each and 4.6 mm pitch was used for calibration purposes. An additional array of  $9 \times 9$  sources (total activity 0.7  $\mu$ Ci), with also 1 mm in diameter but separated by

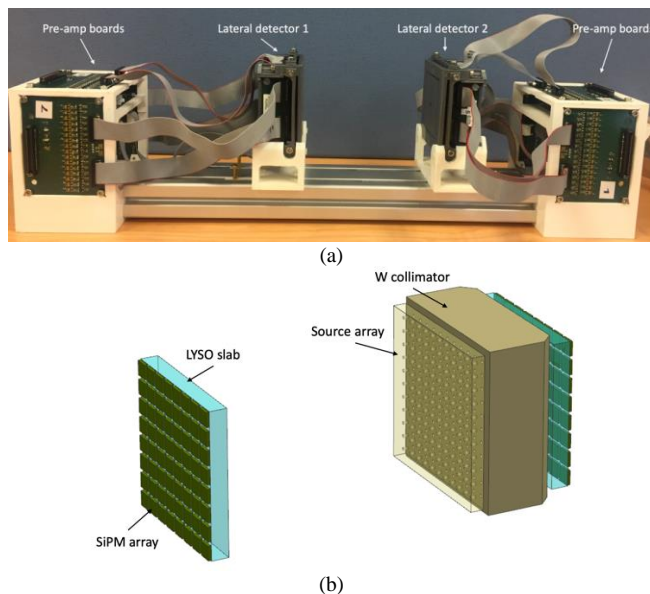


Fig. 2. (a) Photograph of the experimental setup for the lateral reading, showing the two opposite detectors and pre-amplification boards. (b) Sketch of the backreading setup showing the two crystals, the  $8 \times 8$  SiPMs arrays, the Tungsten collimator and the source array.

5 mm, was used for the evaluation of the detector performance. For some tests, the arrays of sources were collimated using a tungsten mask of 24 mm thickness and 1.2 mm diameter drilled holes matching the position of the sources.

### B. Experimental set-up

For coincidence purposes, two identical detector blocks, the detector under characterization and the reference detector, have been mounted at a separation distance (entrance to entrance crystal faces) of 7.5 cm for the lateral reading tests, see Fig. 2 (a). However, for the backreading tests, this distance was increased to 11.5 cm due to mechanical constraints. All measurements have been performed in an opaque black-polystyrene box. A cooling system based on a temperature-controlled air flow has been employed to stabilize the temperature inside the box to  $22 \pm 2$  °C.

For all experiments, the mechanical collimator was placed in between the corresponding array of sources and the detector under study, see Fig. 2 (b). For the calibration measurements, about  $19 \times 10^6$  events were acquired using the  $11 \times 11$  source array. When evaluating the blocks performance, approximately  $4 \times 10^6$  events were acquired using the  $9 \times 9$  source array, due to the low activity of that array of sources.

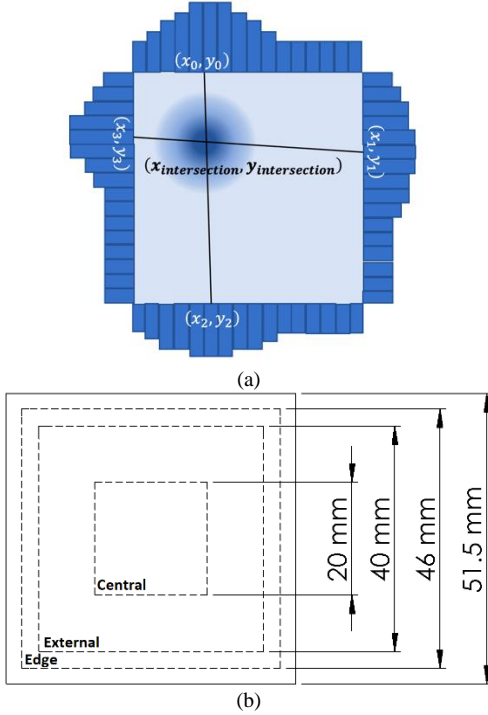


Fig. 3. (a) Sketch of the scintillation crystal and gamma-ray impact. The figure also shows the expected light distributions at each side and the intersection of the lines connecting the two opposite centroids. (b) Sketch of the different regions considered in the crystal for the data analysis.

For the lateral reading tests, the signal of each of the 64 SiPMs (4 arrays of 16 SiPMs) was individually pre-amplified and sent to a data acquisition (DAQ) system. A summed signal of all 16 SiPMs from each array was used for triggering and coincidence detecting. A double leading-edge approach was used to digitize the signals. A true coincidence was generated when the 8 trigger signals (4 laterals for the two detectors in coincidence) were obtained within a coincidence window of 9 ns. After confirmation of a true coincidence, all 128 (64 + 64) signals were digitized using Analog to Digital Converters (ADCs) with 250 ns integration window and 12-bit precision. When the crystal blocks were read out using the larger back

face, the readout electronics provided information for each row and column of the SiPM arrays. For the  $8 \times 8$  SiPMs case, 8 rows and 8 columns were sent to the ADCs for digitation, whereas for the  $16 \times 16$  SiPMs array, 32 signals were digitized.

In detectors based on crystal arrays, the spatial resolution is mainly defined by the pixel size. However, in detector blocks based on monolithic crystals, the detector spatial resolution depends on a variety of factors [10]. Some of them are the crystal geometry, surface treatment, readout electronics and granularity of the photosensor device. Moreover, there exists also a dependence with the type and degree of collimation applied to the data. In our study, different areas of software collimation have been applied to the data. That means that during the data processing, we have allowed only lines of response (LORs) that are almost perpendicular to the crystal surfaces. Therefore, for a given impact position in a detector, the coincidence impact should have occurred within a defined area in the opposite detector. This helps reducing noise, such as random events, and also provides a trend information about the detector intrinsic spatial resolution. This software collimation is only applied during the calibration process explained in section D and for the calculation of the spatial resolution of the detector.

### C. Methods to estimate the interaction position

Four different interaction position estimation methods have been implemented in order to assess the most suitable one for this detector configuration and aspect ratio. In all cases, the measured charge (ADC units) is raised to the power of two before calculation. We have found the convenience of this methodology in prior works [11][12], in order to improve the detectability accuracy, especially near the photosensors. The first method, named *64ch*, calculates the Center of Gravity (CoG) with all 64 signals:

$$x_{64ch} = \frac{\sum_{i=1}^{64} q_i^2 \cdot x^i}{\sum_{i=1}^{64} q_i^2} \quad (1)$$

$$y_{64ch} = \frac{\sum_{i=1}^{64} q_i^2 \cdot y^i}{\sum_{i=1}^{64} q_i^2} \quad (2)$$

where  $q_i$  is the charge collected by the  $i$ -th SiPM and  $(x^i, y^i)$  the mechanical position of that SiPM photosensor. Fig. 3 (a) illustrates a gamma ray impact generating scintillation light reaching the four lateral sides, and the four  $1 \times 16$  SiPMs arrays with their respective charges. Fig. 3 (b) depicts the different regions considered in the crystal for the data analysis.

In the second method, named *intersection* and also illustrated in Fig. 3 (a), the gamma ray interaction point is obtained as the intersection of the two lines connecting the centroids found for opposite faces. The positions  $(x_f, y_f)$ , with  $f = 0, 1, 2, 3$ , are calculated using (1) and (2) but for  $i = 1$  to 16 for each face:

$$\begin{aligned} y_0 &= m_1 \cdot x_0 + n_1 \\ y_2 &= m_1 \cdot x_2 + n_1 \end{aligned} \quad (3)$$

$$\begin{aligned} y_1 &= m_2 \cdot x_1 + n_2 \\ y_3 &= m_2 \cdot x_3 + n_2 \end{aligned} \quad (4)$$

$$x_{intersection} = \frac{n_2 - n_1}{m_1 - m_2} \quad (5)$$

$$y_{intersection} = m_{1,2} \cdot x_{intersection} + n_{1,2}$$

In the third method, named *mean*, the impinging gamma ray position is obtained as the mean value found for the two opposite faces for  $x$  and  $y$ , respectively:

$$\begin{aligned} x_{mean} &= \frac{x_0 - x_2}{2} \\ y_{mean} &= \frac{y_1 - y_3}{2} \end{aligned} \quad (6)$$

In the last approach, the mean value is moreover energy weighted and, therefore, called *weighted*:

$$\begin{aligned} x_{weighted} &= \frac{x_0 \cdot E_0 - x_2 \cdot E_2}{E_0 + E_2} \\ y_{weighted} &= \frac{y_1 \cdot E_1 - y_3 \cdot E_3}{E_1 + E_3} \end{aligned} \quad (7)$$

where  $E$  is the energy deposited in the corresponding lateral side.

For the case of the backreading experiments,  $x$  and  $y$  coordinates were estimated by applying the CoG algorithm of (1) and (2) but to the 8+8 or 16+16 signals (rows + columns), corresponding to the 8×8 or 16×16 SiPMs arrays, respectively.

#### D. Data calibration

A novel methodology based on Voronoi diagrams has been employed for the calibration of planar coordinates ( $x$  and  $y$ ) and energy, for all detector geometries and readouts [13]. This calibration method allows one to correct for the edge effects and for the non-uniformities in the collection of scintillation photons. The detector calibration was carried out by acquiring data with the array of 11×11  $^{22}\text{Na}$  collimated sources. We have calculated the centroid of each calibration source, named calibration points, and the Voronoi diagram of this set of points. The Voronoi diagram is defined as the partitioning of the plane with the 121 calibration points into various convex polygons, named Voronoi cells, with the property that an arbitrary point lies within a specified polygon, if and only if, the distance from this point to the belonging sample of the associated polygon is closer than all other distances between this point and the remaining points. Defining specific  $x$ ,  $y$  and energy calibration factors for each Voronoi cell and applying an interpolation method (Natural Neighbouring in this work) we obtain the underlying calibration map. This calibration map is used to correct the estimated gamma ray interaction positions and energy for any measurement. Notice that we have carried out the detector calibration for each readout and position estimation algorithm.

#### E. Spatial resolution

The spatial resolution is determined by the mean value of the Full Width at Half Maximum (FWHM) of the measured sources

profiles. We have determined the FWHM of all sources by fitting multi-Gaussian profiles to all rows and columns of sources. This was carried out for the 9×9 sources array, after calibration. We have calculated the average spatial resolution ( $x$  and  $y$  direction) for the central and for the external regions, as shown in Fig. 3 (b). Different degrees of software collimation have been evaluated in order to provide information about the expected intrinsic spatial resolution of the detector block. An energy filter of 400 - 600 keV has been applied to all data. For some cases, we have also investigated the effect on the spatial resolution of extending the energy filter to 100 – 600 keV.

#### F. Energy resolution

The energy resolution has been measured without the mechanical tungsten collimation having the 11×11 sources array at a distance of 4 cm from the detector under study, working as a uniform radiation source. For each coincident event, the signals of the 64 SiPMs of the detector have been summed up and histogrammed. The photopeak centroid and FWHM values have been obtained by fitting a Gaussian distribution together with a decay exponential. This exponential function helps to determine those parameters more accurately. The photopeak position has been obtained for the non-calibrated data, whereas the energy resolution was obtained after the calibration. In addition to the energy resolution as a function of the impact position, we have calculated the mean value for the central, external and edge regions.

#### G. Nuclear and optical simulations

An optical simulation has been carried out using GATE v8.1 to shed light on which method estimates better the impact position when compared to the real interaction position. The simulation considers a LYSO block, with identical dimensions and treatment to the experiment. In particular, we used the *lutESR* treatment defined by GATE. The light collected at each lateral side was sampled in 16 bins recreating the SiPMs array. A SiPM photon detection efficiency of 50% was considered during the simulation, but not the SiPMs dark count rates. A  $^{22}\text{Na}$  source was placed at 5 mm from the crystal surface, and  $15 \times 10^3$  events were collected.

To determine the goodness of each method we calculated the interaction position ( $x'$ ,  $y'$ ) of each simulated event and compared it with the interaction position ( $x$ ,  $y$ ) given by the nuclear simulation. The calculated position is obtained for the four approaches described in section C with the simulated information of the charges collected at each lateral side. In the case that a simulated event involves multiple interactions within the crystal (one or multiple Compton events and photoabsorption), the interaction position is obtained as the mean value of the positions of each interaction, but energy weighted. The comparison between the interaction position and the calculated position was determined by the difference between these two values (bias) versus the interaction position. An energy filter of 400-600 keV was applied to the data.

### III. RESULTS

#### A. Data calibration

Fig. 4 shows both the calibration and validation data, before and after applying the calibration method explained in section II.D, using the four impact determination approaches described in section II.C. From top to bottom, *64ch*, *intersection*, *mean* and *weighted* cases. From left to right,  $11 \times 11$  non-calibrated sources,  $11 \times 11$  calibrated,  $9 \times 9$  non-calibrated, and  $9 \times 9$  calibrated sources. Notice that except for the *64ch* case, all other cases show certain overlapping of sources at the edges when using the  $11 \times 11$  array (covering  $46 \times 46$  mm<sup>2</sup>, scintillator  $51 \times 51$  mm<sup>2</sup>). This is a reason to use a slightly smaller array for the validation ( $9 \times 9$ , covering  $40 \times 40$  mm<sup>2</sup>). For a proper illustration of the flood maps shown in Fig. 4, different values of smoothing, saturation and noise suppression have been applied. However, for the analysis of the data none of these parameters have been applied.

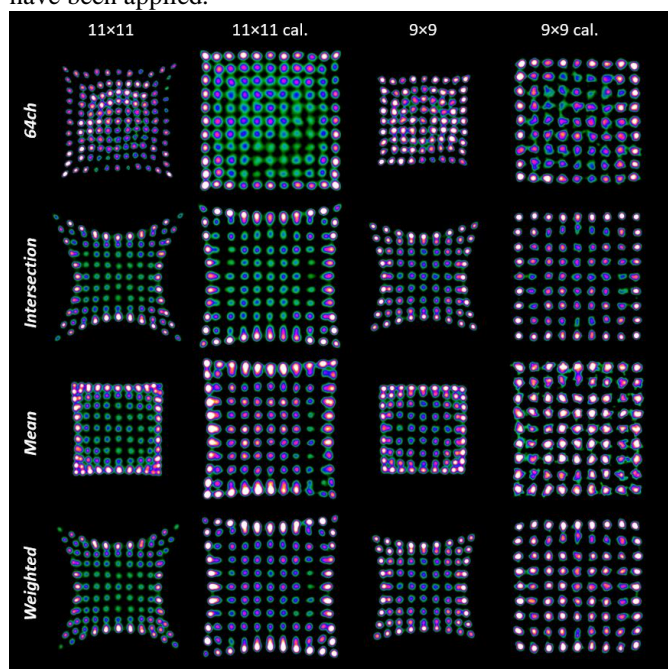


Fig. 4. Calibration and validation data. From top to bottom: *64ch*, *intersection*, *mean* and *weighted* cases, respectively. From left to right: non-calibrated  $11 \times 11$  sources array, Voronoi calibration of the  $11 \times 11$  sources array, non-calibrated  $9 \times 9$  sources array, Voronoi calibration of the  $9 \times 9$  sources array.

#### B. Simulation

Fig. 5 depicts the difference (bias) between the interaction position given by the nuclear simulation and the calculated interaction position after collection of the simulated scintillation light in the 64 lateral SiPMs, as a function of the interaction position, and for the four position methods described in section II.C. The results obtained show that the *64ch* approach is the interaction position estimation method that provides the smallest bias. Indeed, this allows to recover the  $11 \times 11$  sources both in the uncalibrated and calibrated images of Fig. 4 without any overlapping of sources. All other methods exhibit an increasing bias from the center towards the edges of the crystal.

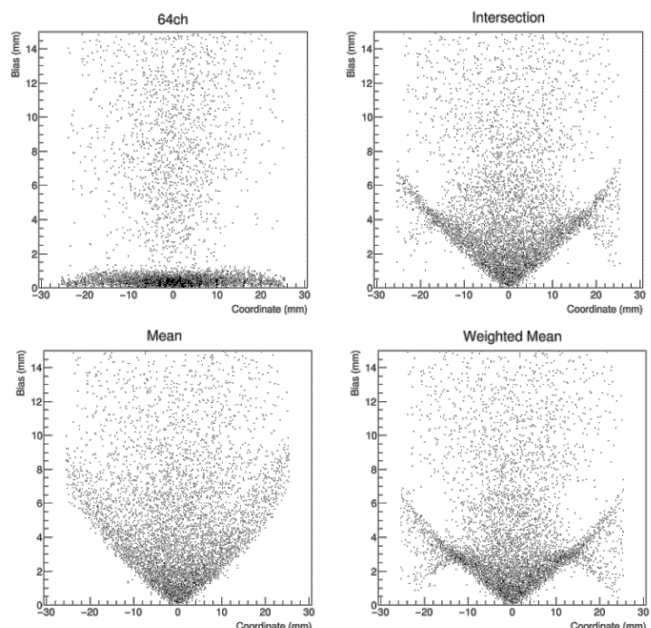


Fig. 5. Difference between the calculated interaction positions ( $x'$ ,  $y'$ ) and the interaction positions ( $x$ ,  $y$ ) given by the simulation for the four position estimation methods applied.

#### C. Spatial resolution

In Fig. 6 we summarize the results obtained concerning the spatial resolution FWHM for the four position estimation methods, after calibration, for the  $x$  and  $y$  coordinates. The results are presented as a function of the degree of collimation. In the plots we show the results for all  $9 \times 9$  sources ( $40 \times 40$  mm<sup>2</sup>). They also depict the results for the central and external regions, accounting for  $5 \times 5$  sources ( $20 \times 20$  mm<sup>2</sup>) and the remaining sources, respectively, as depicted in Fig. 3 (b).

The measured spatial resolution increases with the area of collimation, as expected [10]. The most uniform results for the total, center and external regions are obtained for the *weighted* case (Fig. 6). The results that exhibit more variation among these regions are found for the *64ch* approach. The *intersection* method tends to show the best FWHM values of 1.7 mm for the smallest area of collimation of 4 mm<sup>2</sup>. We can observe that only in the case of the *mean* method the resolution in the external region is worse than the one in the center.

By extrapolating the curves shown in Fig. 6 to zero collimation, one can estimate the intrinsic spatial resolution, without accounting for the source dimension (1 mm in diameter) [10]. We have calculated these values by fitting the curves containing the total data (curve with black squares) in Fig. 6 to a logarithm function of the type  $y = b \cdot \ln(x - a)$ . This function does not have any physical meaning, but follows well the data distribution. From these curves, we finally obtained a value at a collimation area of 0 mm<sup>2</sup> for the *64ch*, *intersection*, *mean* and *weighted* cases of 2.2 mm, 1.6 mm, 2.1 mm and 1.7 mm, respectively.

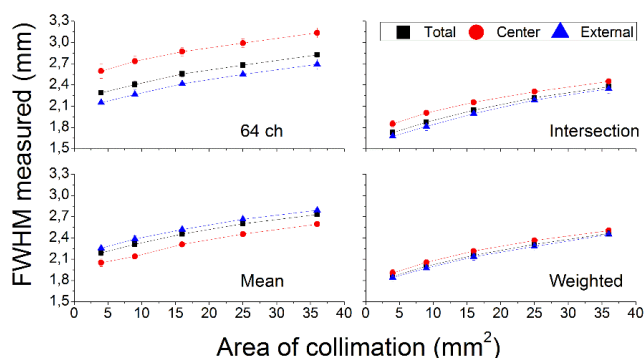


Fig. 6. Spatial resolution FWHM for the whole crystal, central and external sources, as a function of the different position estimation methods and software collimation.

Fig. 7 depicts the flood maps for the average spatial resolutions as a function of the impact position, for all methods and for the 4 mm<sup>2</sup> software collimation. In general, the spatial resolution is better in the external region than in the central one, except for the *mean* case, as we can also observe in Fig. 6. However, the FWHM distribution is more homogenous for this case.

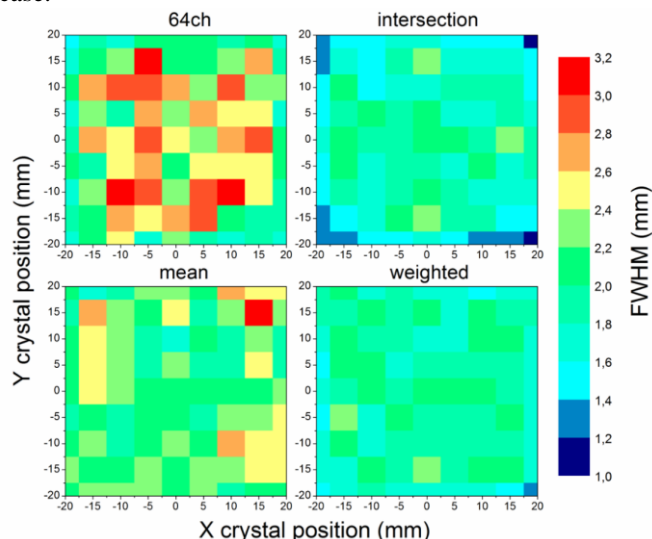


Fig. 7. Flood maps with the average ( $x$  and  $y$ ) spatial resolutions obtained with the  $9 \times 9$  sources array calculated with the four position estimation methods under study applying 4 mm<sup>2</sup> software collimation.

Although the results for the *64ch* case show the highest measured FWHM values, this method allows one to resolve the 100% of events without overlapping at the edges (see Fig. 4). Therefore, for this approach, we have additionally evaluated the spatial resolution (FWHM) for the crystal edge using the  $11 \times 11$  sources array, but only for a software collimation of 9 mm<sup>2</sup>. We choose this area of collimation as a compromise between spatial resolution and statistics. For the sources at the edge (only 2.75 mm to the photosensor) we obtain an average spatial resolution of  $1.48 \pm 0.15$  mm (see Fig. 8). We observe certain degradation of the FWHM at the center of the crystal, as found in Fig. 7. Note that slightly different values are obtained when compared to this figure, since the pitch for this array is just 4.6 mm (compared to 5 mm in Fig. 7).

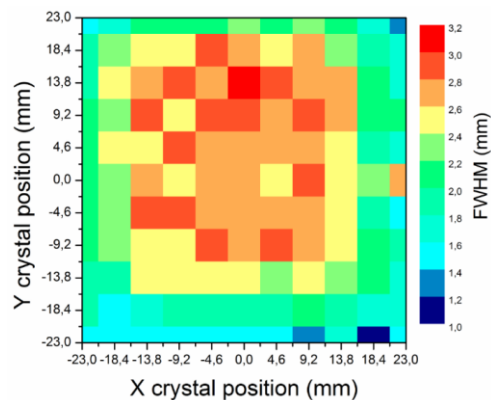


Fig. 8. Flood map with the spatial resolutions obtained with the  $11 \times 11$  sources array calculated with the *64ch* method applying 9 mm<sup>2</sup> software collimation.

We have also investigated the effect on the spatial resolution of extending the energy filter applied to the data to lower energies. The evaluation has been performed with data obtained with the  $11 \times 11$  sources array, for the *64ch* case and applying a software collimation of 9 mm<sup>2</sup>. Two different energy filters have been applied to the detector and to the reference detector, namely *photopeak* (400 – 600 keV) and *full energy* (100 – 600 keV). The results obtained for central, external, edge and all sources are summarized in Fig. 9. These results show that the spatial resolution degrades when lower energies are considered in both detectors, around 12% when all sources are considered.

Regarding the DOI resolution ( $z$  coordinate) of the proposed detector geometry, it corresponds to the crystal thickness, being 3 mm.

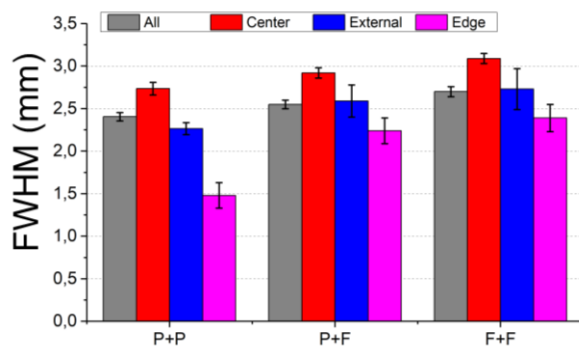


Fig. 9. Spatial resolutions obtained with different energy windows, namely *photopeak* (P, 400 – 600 keV) and *full energy* (F, 100 – 600 keV). Left: photopeak applied to both detectors. Center: photopeak applied to the reference detector and full energy applied to the detector. Right: full energy applied to both detectors.

#### D. Energy resolution

The energy resolution was evaluated for the calibrated data using the *64ch* case. The results should not change independently of the method, but this case allowed one to obtain the photopeak gain and energy resolution for the whole  $51.5 \times 51.5$  mm<sup>2</sup> scintillation area, since there is not overlap of sources neither before or after calibration. Fig. 10 (a) and Fig. 10 (b) show the normalized photopeak position and the energy resolution for different gamma ray incidence positions, respectively. The maximum gain spread among the detector is

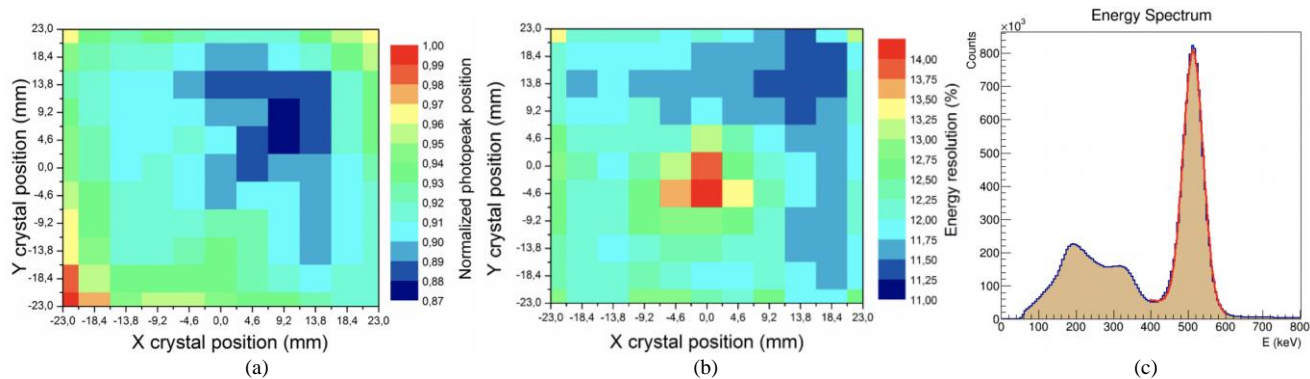


Fig. 10. Flood maps obtained with the  $11 \times 11$  sources array with the average (a) normalized photopeak positions and (b) energy resolutions as a function of the impact position. (c)  $^{22}\text{Na}$  spectra for the whole detector block.

13%. The analysis of the energy resolution resulted in  $12.1 \pm 0.1\%$  FWHM for the entire block (Fig. 10 (c)),  $12.7 \pm 0.1\%$  for the central region and  $11.8 \pm 0.1\%$  for sources at the external region. As we have done for the spatial resolution, by analysing only the sources at the edge region, we obtained an energy resolution of  $12.2 \pm 0.1\%$ .

### E. Backreading comparison

The results shown in the above sections have been compared to the case of using photosensors coupled to one of the large faces of the crystal, namely backreading approach. The *64ch* method has been employed to process the data obtained for both the lateral and the backreading approaches. We selected the *64ch* case since it improves the resolvability for the whole block, but also exhibited the less position dependence both in the experiments and simulations. The software collimation applied to the lateral reading data was  $3 \times 3 \text{ mm}^2$ . The equivalent area of collimation applied to the backreading data was calculated considering that in these last experiments the separation between the crystals was 11.5 cm instead of 7.5 cm (see section II.B), suggesting an area of collimation of  $4.6 \times 4.6 \text{ mm}^2$ . The data sets obtained for the backreading contained  $1 \times 10^6$  events for the  $8 \times 8$  SiPM array set-up and  $0.5 \times 10^6$  events for the  $16 \times 16$  SiPM array configuration, acquired with the  $9 \times 9$  sources array. Once we applied the software collimation and filtered by energy both data sets had the same number of events, so the results for the spatial resolution are comparable.

Fig. 11 shows at the left and right hand-sides the flood maps for the measured FWHM spatial resolution using the  $8 \times 8$  and  $16 \times 16$  SiPM configurations, respectively. Here we show the average FWHM value for the  $x$  and  $y$  axes. We observe that better spatial resolutions are obtained for the photosensor and readout using  $16 \times 16$  SiPMs, as expected.

Regarding the energy response of the three configurations, Fig. 12 shows the energy profiles of the whole detector. This figure also depicts the fit to the distribution. We have compared the results obtained for the lateral with the two backreading approaches. The backreading experiments exhibited values of 12.8% and 14.3% FWHM for the  $8 \times 8$  and the  $16 \times 16$  detectors, respectively, whereas the lateral reading resulted in 11.7%, similar to the value shown in section D obtained as the average of the 121 sources (12.1%).

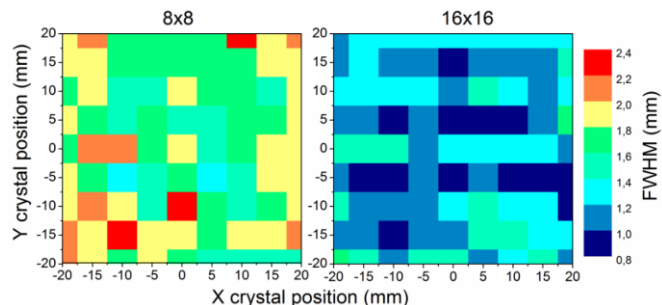


Fig. 11. Flood maps with the measured spatial resolution FWHM for the backreading experiment using the  $8 \times 8$  SiPMs array (left) and for the  $16 \times 16$  SiPMs array (right).

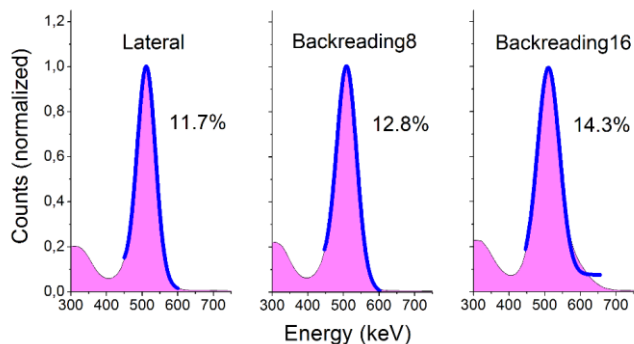


Fig. 12. Energy plots for the whole detector blocks and fit (solid blue line) for the lateral reading (left), backreading using the  $8 \times 8$  SiPM array (center) and when using the  $16 \times 16$  SiPM array (right).

Fig. 13 shows the contour plots for the photopeak position and energy resolution for different gamma ray incidence positions for the two backreading cases namely  $8 \times 8$  and  $16 \times 16$  SiPM configurations. Both cases show gain spreads as large as about 12% and 16%, for the  $8 \times 8$  and  $16 \times 16$  SiPM configurations, respectively. A slightly more uniform response is observed for the  $8 \times 8$  case. The  $16 \times 16$  configuration exhibited certain deterioration of the energy resolution at the very edge regions of the crystal.

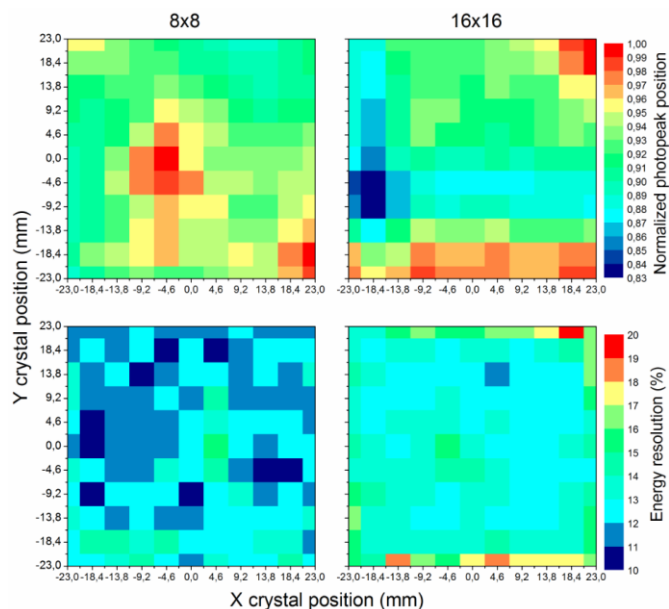


Fig. 13. Energy performance of the backreading tests. Top panels show the gain dependency with the impact position. Bottom panels exhibit the energy resolution as a function of the impact position.

Fig. 14 summarizes and compares the results obtained for the spatial and energy resolutions. The plot on the left-hand side depicts the comparison of the measured FWHM spatial resolution between the three set-ups. Here, we observe that using the higher density of photosensors (256 SiPMs) improves the detectability (spatial resolution). Regarding the energy resolution, in contrast to the measured spatial resolution, more similar values are obtained independently of the used photosensor configuration (lateral or backreading). Moreover, worse results are observed for the highest density photosensor case.

#### IV. DISCUSSION

We have evaluated wide LYSO scintillation crystals with very high aspect ratio that could be used in PET detector configurations based on multiple layers. This approach would benefit the identification of Compton and photoelectric events in different layers, allowing one to use not only standard LORs during the reconstruction process but also Compton kinematics.

We made it possible to collect the scintillation light using

photosensors located at the lateral sides of the crystal using custom arrays of  $1 \times 16$  SiPMs. The aspect ratio of our design is 17.2, compared to prior experimental works following a similar methodology of 4.8 [7] or 9.1 [6]. This very high aspect ratio could cause some performance deterioration of the detector block due to the very long travel paths of the scintillation photons.

We have deeply worked on the most proper way of estimating the impact position with the information provided by the 4 side SiPM arrays. Simulation data helped to identify that the *64ch* approach returned a very small average bias, and very small spread of it. The measured data with the calibration array already exhibited a very good performance of the *64ch* method, improving resolvability power especially near the photosensors. We have empirically estimated a maximum limit of the intrinsic spatial resolution as good as 1.6 mm for the *intersection* case, and about 2.2 mm for the *64ch* approach, being the best and the worst cases, respectively. These values still contain the source dimensions. Differently from another work [6], this was obtained without the need for optical barriers, and the current results are rather homogeneous across the whole detector surface due to the corrections performed by the calibration process.

Regarding the energy resolution, we have found values close to or better than state-of-the-art detector blocks based on crystal arrays. We reached about 12% FWHM energy resolution with a very small impact position dependency. Simulations carried out in [3] showed that energy resolutions of the order of 10% FWHM might be of use in determining the Compton kinematics. In this sense, faster and brighter scintillator crystals could be used, namely  $\text{LaBr}_3$ ,  $\text{CeBr}_3$  or Calcium co-doped Lutetium based types. Most likely, those type of crystals could allow for a more accurate determination of the Compton cones [3][14]. However, due to their hygroscopic nature and associated mechanical restrictions, their use could result more limited [15].

The comparison between lateral reading and backreading detectors has shown that the spatial resolution obtained with both backreading approaches overcomes the performance of the lateral reading, as much as a factor 2 in some cases. When examining the energy response, we found a slightly better resolution for the lateral case (11.7%) than for the backreading

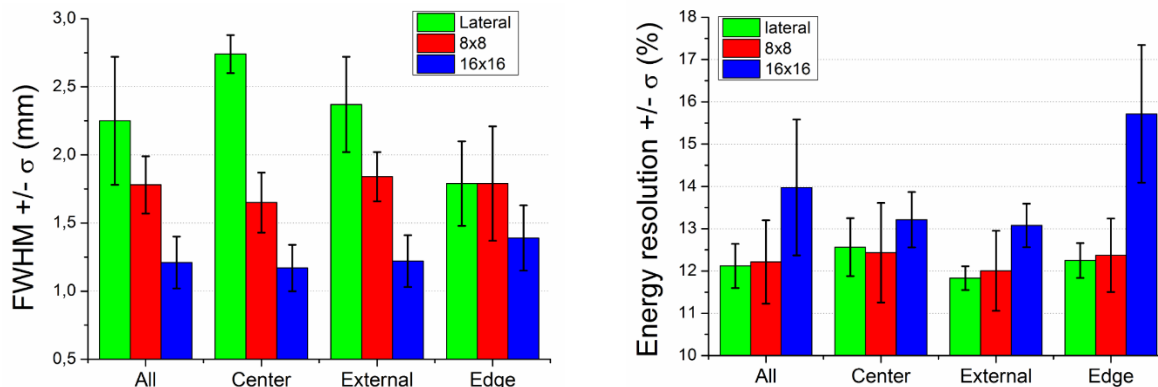


Fig. 14. Comparison of the results obtained with the three experiments. Left, spatial resolution. Right, energy resolution.

case (12.8% and 14.3%).

Notice that in the case of the lateral reading, there is a significant reduction of the photosensor area when compared to the standard backreading approach. In particular, we have used 4 arrays of  $1 \times 16$  elements of  $3 \times 3$  mm<sup>2</sup> each, giving a total of 576 mm<sup>2</sup> of SiPM sensitive surface. When using back reading approaches, this value increases to 2304 mm<sup>2</sup> ( $16 \times 16$  SiPMs of  $3 \times 3$  mm<sup>2</sup> or  $8 \times 8$  SiPMs of  $6 \times 6$  mm<sup>2</sup> each). Therefore, we are saving about three-fourths of the corresponding photosensor material. Hence, lateral readout makes sense from the economical point of view only if the area of the slab is large compared to its thickness (total number of SiPM detectors of the lateral surface proportional to  $4 \times L \times T$ , where L and T stand for Length and Thickness, respectively, compared to  $L \times L$  for conventional back readout).

The DAQ system employed in the characterization of these detector blocks has intrinsic timing resolution capabilities around 2-3 ns. This value prevents the measurement of accurate timing information and this is the reason why the detector characterization presented in this paper does not include any timing measurement. To overcome this limitation, it is planned to substitute the readout electronics by the TOFPET2 ASIC from PETsys Electronics (Lisbon, Portugal).

## V. CONCLUSIONS

In this work, we have investigated the capability to only use 64 SiPMs placed at the lateral sides of a wide LYSO scintillator slab. Although the aspect ratio of our design is very high (above 17), we have made it possible to reach an intrinsic spatial resolution of 1.6 mm with an energy resolution of about 12%. This overall detector block performance allows us for an accurate identification of the gamma-ray impact coordinates and energy for the whole crystal volume of both photoelectric and Compton interactions in order to use them for the reconstruction process in systems based on multilayer configurations, especially for molecular imaging such as PET scanners.

## REFERENCES

- [1] J. van Sluis, et al., "Performance characteristics of the digital Biograph Vision PET/CT system," *J. Nucl. Med.* 2019, doi:10.2967/jnumed.118.215418
- [2] P.R.R.V. Caribe, et al., "NEMA NU 2-2007 performance characteristics of GE Signa integrated PET/MR for different PET isotopes," *E. J. Nucl. Med. Mol. Imag.* 6, 598, 2019.
- [3] V. Ilisie, et al., "Building blocks of a multi-layer PET with time sequence photon interaction discrimination and double Compton camera," *Nucl. Instrum. Meth. A* 895, 2018.
- [4] A. Studen et al., "First coincidences in pre-clinical Compton camera prototype for medical imaging". *Nucl. Instr. Meth. A* 531, 258, 2014.
- [5] S. Takeda et al., "Applications and Imaging Techniques of a Si/CdTe Compton Gamma-Ray Camera" *Physics Procedia* Volume 37, 2012, Pages 859-866.
- [6] X. Li, et al., "An edge-readout, multilayer detector for positron emission tomography," *Med. Phys.* 45, 2425, 2018.
- [7] P. Peng, et al., "Compton PET: a layered structure PET detector with high performance," *Phys. Med. Biol.* 64, 10LT01, 2019.

- [8] J.M. Benlloch, F. Sanchez and A.J. Gonzalez, Compton gamma-ray camera system with time-of-flight measurement, WO2017077164A1, 2015.
- [9] A.J. Gonzalez, F. Sanchez and J.M. Benlloch, "Organ-Dedicated Molecular Imaging Systems," *IEEE Trans. Rad. Plasma Med. Sci.* 2, 388, 2018.
- [10] A. Gonzalez-Montoro, et al., "Novel method to measure the intrinsic spatial resolution in PET detectors based on monolithic crystals," *Nucl. Instrum. Meth. A* 920, 2019.
- [11] A.J. Gonzalez, et al., "A PET Design Based on SiPM and Monolithic LYSO Crystals: Performance Evaluation," *IEEE Trans. Nucl. Sci.* 63, 2471, 2016.
- [12] Pani, et al., "Preliminary evaluation of a monolithic detector module for integrated PET/MRI scanner with high spatial resolution," *J. Instrum.* 10, C06006, 2015.
- [13] M. Freire, et al., "Calibration of Gamma Ray Impacts in Monolithic-Based Detectors Using Voronoi Diagrams," *IEEE Trans. Rad. Plasma Med. Sci.*, vol. 4, no. 3, pp. 350-360, 2020.
- [14] J. Barrio, et al., "Performance improvement tests of MACACO: A Compton telescope based on continuous crystals and SiPMs," *Nucl. Instrum. Meth. A* 912, 2018.
- [15] J. Barrio, et al., "Characterization of LYSO and CeBr<sub>3</sub> Detectors with Lateral Sides Readout for a Multilayer Compton-PET," 2019 IEEE NSS/MIC CR, 2019, pp. 1-3, doi: 10.1109/NSS/MIC42101.2019.9059991.